Engineering Fracture Mechanics 276 (2022) 108833

Contents lists available at ScienceDirect

Engineering Fracture Mechanics

journal homepage: www.elsevier.com/locate/engfracmech

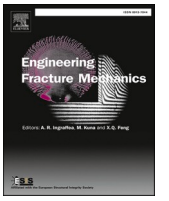

Mixed-mode dynamic fracture behavior of a rubber toughened epoxy adhesive under stress wave loading

A. Taylor Owens *, Hareesh V. Tippur

Department of Mechanical Engineering, Auburn University, AL 36830, United States

ARTICLE INFO

Keywords:
Epoxy adhesives
Dynamic fracture
Mixed-mode
Semi-circular beam geometry
Digital image correlation
Finite element model

ABSTRACT

This work seeks to measure mixed-mode fracture parameters for a dynamically growing crack in a core shell rubber toughened epoxy adhesive (EPON™ 828 with PARALOID™ EXL-2691J particles). Digital image correlation technique coupled with ultrahigh-speed photography and a hybrid finite element-based post-processing approach are used to extract fracture parameters. The dynamic loading is accomplished by using a striker to induce stress waves in an incident bar in contact with a free-standing semi-circular specimen. A companion finite element analysis is performed for investigating suitable experimental parameters and configurations for implementing the approach and determining specific experimental parameters (crack length, crack angle, and impact velocity) necessary to achieve the desired experimental conditions (mode mixity at crack initiation and strain rate). The critical fracture parameters are used to generate mixed mode fracture envelope and fracture toughness-mode mixity relationship for the material. Further investigation is carried out to evaluate various fracture criteria for predicting initial crack kink angles. The measured dynamic fracture quantities are also compared with the quasi-static counterparts to assess strain rate-dependence of the adhesive. The results reveal a decrease in critical stress intensity factors of approximately 10 % and 30 % for the mode I and mode II states, respectively, with increasing strain rate. Post-initiation, the dynamic crack propagates at a near-constant mode I stress intensity factor of ~1.4 MPa-$\sqrt{m}$. Under dynamic conditions, the critical, effective stress intensity factors are relatively constant with respect to mode mixity. This is in contrast to quasi-static results where the effective values increased with respect to mode mixity. Experimentally measured crack kink angles agree well with those predicted by the maximum energy release rate criteria and the maximum tangential stress criteria, particularly under mode I dominant conditions.

1. Introduction

Fiber-reinforced composite materials have found widespread usage in recent years, generally enabled by a better understanding of their thermal and mechanical characteristics and an overall progress with respect to processing and manufacturability. However, certain challenges remain. Due to their inherently low bearing strength, traditional methods of fastening using bolts, screws, or rivets is challenging, often requiring significant additional material thickness. Therefore, it is frequently advantageous to make structural attachments via secondarily bonded adhesive joints. Thus, fracture behavior of polymer adhesives is particularly important in this

* Corresponding author.
E-mail address: owensat@auburn.edu (A. Taylor Owens).

https://doi.org/10.1016/j.engfracmech.2022.108833
Received 5 July 2022; Received in revised form 21 August 2022; Accepted 21 September 2022
Available online 27 September 2022
0013-7944/Published by Elsevier Ltd.

Nomenclature

a	Crack length
A	Area encompassed in domain integral calculations
ASTM	American Society for Testing and Materials
B	Specimen thickness
cc	Cubic centimeters
C	Celsius
DIC	Digital Image Correlation method
DSR	Decompose, Shift, Reconstruct method
F	Static specimen load
$F(t)$	Dynamic force history applied to specimen
FE	Finite elements
g	grams
G	Strain energy release rate
GPa	Gigapascals
Hz	Hertz
J	J-integral
kN	kilo Newton
K_I, K_{II}	Mode I and Mode II stress intensity factors
K_{EFF}	Effective stress intensity factor
LS	Least squares
m	meters
mm	millimeters
min	minute
MHz	Megahertz
MPa	Megapascals
MTS	Maximum Tangential Stress criteria
MERR	Maximum Energy Release Rate criteria
r	Radial position in crack tip coordinate system
R	Specimen radius
s	Seconds
S	Specimen support span
T_x, T_y	Specimen rigid body translations
u_x, u_y	Sliding and opening displacement in crack tip coordinate system
W	Strain energy density
Y_I, Y_{II}	Normalized Mode I and Mode II stress intensity factors
β	Specimen crack angle relative to horizontal edge of specimen
σ_{ij}	Stress tensor
μ	Shear modulus
$\mu\varepsilon$	Microstrain
θ	Angular dimension in crack tip coordinate system
Ω	Resistance in Ohms
υ	Poisson's ratio
°	Degrees

regard. Design and analysis of these types of joints requires an understanding of mixed mode fracture behavior of the adhesive due to complex stress distribution in the adhesive layer. Additionally, structural and thermal loads can occur over a broad range of timescales and the polymeric constituents that make up composite laminates and adhesives exhibit time-dependent responses.

While a great deal of attention has been given to the study of the mode I fracture problem under dynamic initiation and propagation conditions, for instance, the noteworthy work by Ravi-chandar and Knauss [1], a more limited amount of work has been devoted to mixed-mode fracture problems. One work [2] utilized an eccentrically loaded 3-point bending specimen coupled with coherent gradient sensing to characterize mixed-mode fracture of PMMA. The Brazilian disc geometry was used for investigation of mixed-mode fracture by a few previous authors including that presented in [3]. This approach, however, has its challenges in that the two crack tips that are present in the specimen introduce difficulty in terms of which of the two would initiate first. Having two separate crack propagation events invariably creates asymmetry during crack growth. More recently, Gao, et al. [4] introduced a method to utilize the notched semi-circular geometry with three-point support and loaded in a split-Hopkinson bar setup for mode I fracture parameter extraction. They proposed that the transmitter bar strains be used to compute the force balance in the test specimen for stress intensity factor calculation. Their work, however, does not address mixed-mode fracture. Very limited, if any, work is reported in the literature

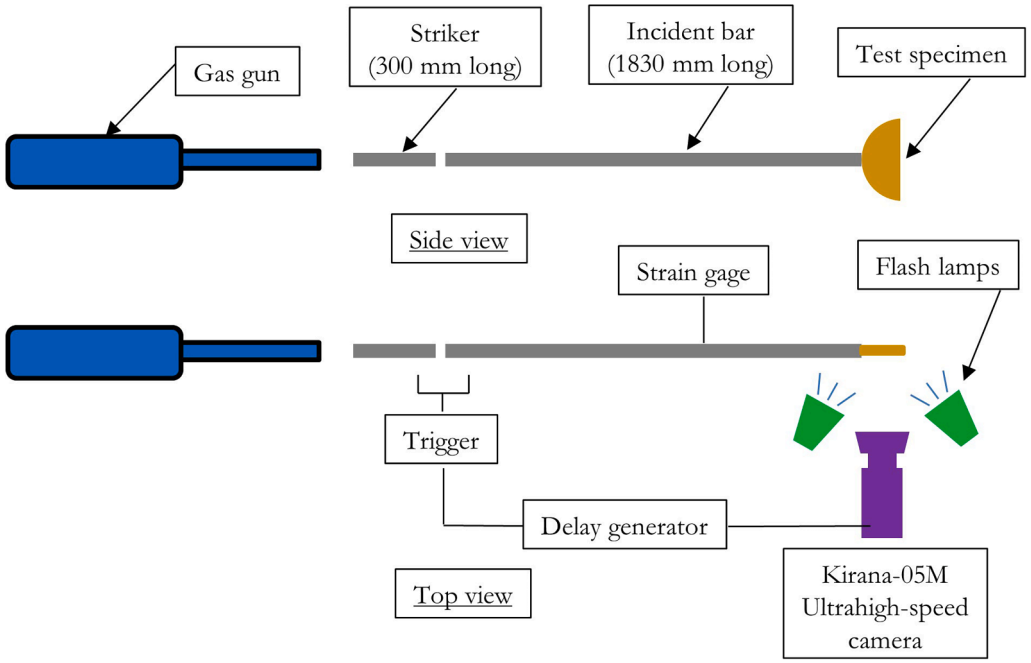

Fig. 1. Experimental setup (side view and top view) of stress wave loading apparatus for dynamic mixed-mode fracture.

that investigates dynamic fracture across a full expanse of mode mixities for different strain rates using a single test specimen geometry that is also conducive to full-field measurements.

With respect to rubber-toughened epoxies, Kinloch, et al. [5] investigated the quasi-static mode I fracture response with a focus on microstructural evaluation and identification of various potential toughening mechanisms. The work was followed by a separate study [6] to include characterization of rate-dependent effects at different but low strain rates. A study was later performed by Pearson and Yee [7] to investigate the effects of particle size on the toughening of rubber-modified epoxies. Their work contributed to the understanding of microstructural effects of rubber particles in mode I fracture. A particularly comprehensive review was published by Baheri, et al. [8] documenting the history of the usage of rubber to toughen epoxies and a quite extensive survey of the literature with respect to characterization of the effects on toughness.

Regarding techniques used to extract fracture parameters using full-field measurements, two-dimensional digital image correlation (DIC) technique for quantifying displacement fields has achieved popularity in recent years. The method was introduced in the early 1980's but has evolved to include both 2-D and 3-D measurements [9–12]. The general principle involves applying a random pattern to the surface of an object in the region of interest. As mechanical loads are imposed on the object, the random pattern/speckles follow the deformation of the surface of the object being tested. Image processing techniques are subsequently used to track the surface motion and local deformation. The method is widely documented with a particularly thorough exposition of the technique and its applications in [13]. Several prior authors have implemented methods to utilize full-field displacement measurements to understand material fracture. Sanford [14,15] introduced one approach that has been widely used that utilizes an over-deterministic least-squares error minimization technique based on full-field optical measurements and analytical stress field solutions for evaluating opening-mode

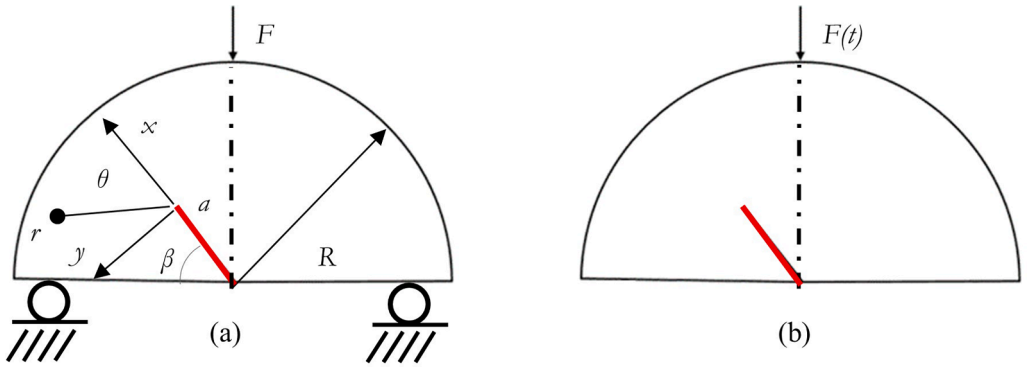

Fig. 2. Semi-circular beam bending test configuration for (a) static and (b) dynamic experiments.

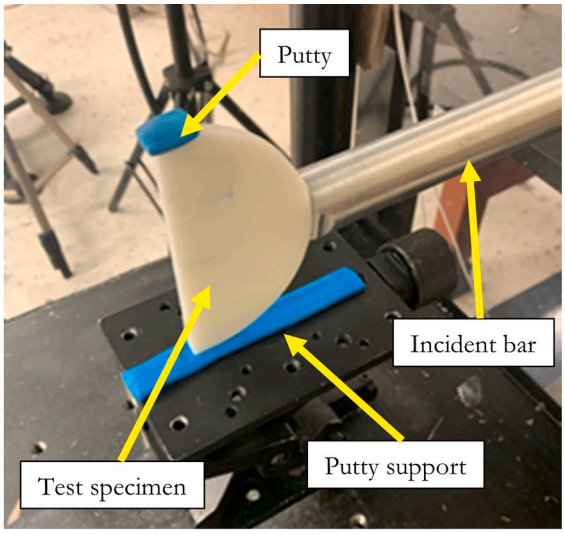

Fig. 3. Detailed image of specimen in dynamic fracture experimental setup showing support details and incident bar contact.

stress intensity factors in cracked specimens. Other authors [16–18] have reported utilizing measured displacements from digital image correlation in conjunction with least-squares regression analysis to identify fracture parameters. DIC was used with a flexural impact setup to investigate particle-filled epoxy under mixed-mode fracture conditions in [19]. With respect to the dynamically propagating crack problem, Kirugulige [20] extended one of these approaches to the investigation of mixed mode behavior under dynamic loading conditions. Yoneyama [21] demonstrated the extraction of the *J*-integral from a cracked specimen using displacement data from digital image correlation. Yates, et al. [22] investigated the effects of fatigue on cracked specimens using the least-squares approach with displacements from digital image correlation method to extract fracture quantities to include the so-called *T*-stress values.

In this context, the primary objective of the current work is to investigate the merits of a single edge cracked semi-circular beam

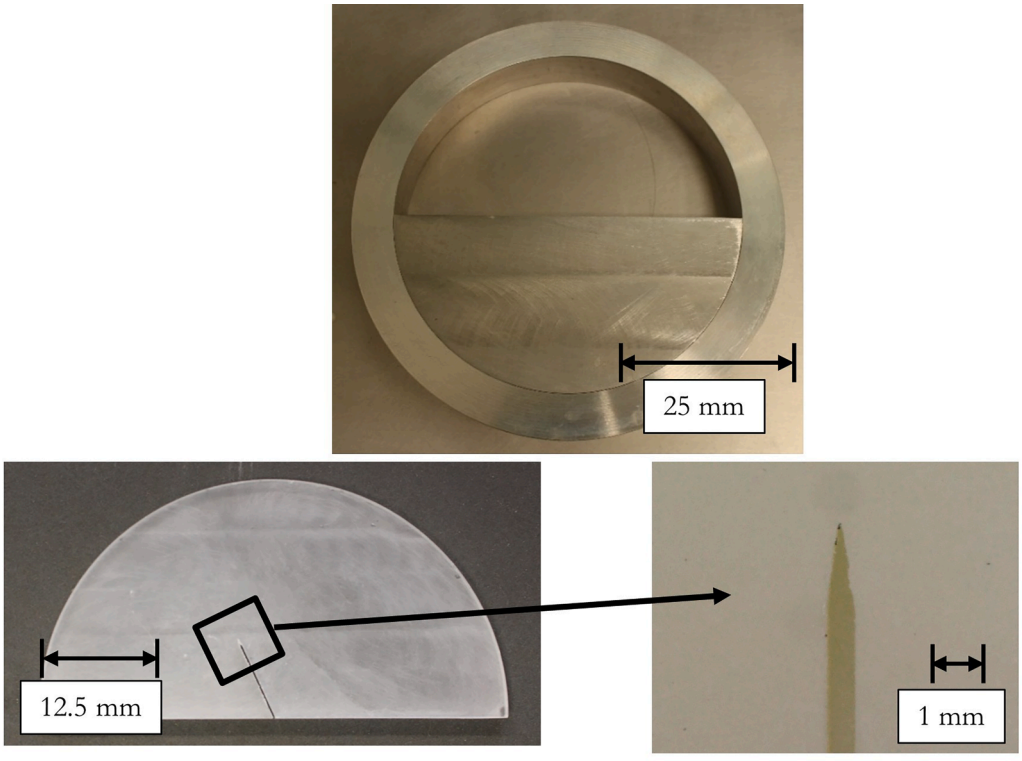

Fig. 4. Specimen mold (top), cast sample with an inclined crack (lower left) and close-up of the crack tip produced by razor blade (lower right).

geometry in a single-point stress wave loading configuration for studying mixed-mode dynamic fracture from mode I to mode II. Quantifying the strain rate dependent behavior of an epoxy toughened with a core shell rubber particles is a secondary objective. Details of the experimental setup are discussed first in this paper to include specifics about the material being tested, the specimen geometry, and specimen preparation details. The procedure for extracting fracture parameters from full field displacement measurements using a hybrid finite element based approach is critically examined next. Dynamic fracture behavior of the rubber toughened epoxy adhesive material is then studied and compared to its quasi-static counterparts.

2. Experimental details

2.1. Experimental setup

To evaluate the fracture quantities of interest, a long bar apparatus was utilized for subjecting the test specimen to single-point dynamic loading. The test setup is shown schematically in Fig. 1. In this setup, a gas gun is used to accelerate a 305 mm long, 25.4 mm diameter 7075-T6 aluminum striker bar up to the desired velocity. The striker bar is propelled towards a 1.83 m long, 25.4 mm diameter 7075-T6 aluminum long bar. The striker, upon impacting the incident bar, generates an elastic wave that propagates the length of the long bar into the test specimen. A strain gage located on the long bar enables measurement of the incident and reflected stress waves. A trigger and a delay generator are used to control the image acquisition through a Kirana-05 M ultrahigh-speed camera. The camera is equipped with a 924 × 768 sensor with 10-bit gray scale resolution. A Nikkor 80–400 mm focal length macro zoom lens with a focal length doubler is utilized. The camera is equipped to acquire 180 images of the dynamic event at up to 5 million frames per second.

2.2. Test specimen geometry and loading configuration

The semi-circular beam (SCB) test specimen geometry was first introduced to study mechanics problems involving cored concrete and rock [23–25] cylinders. However, the geometry has found much more widespread usage across a range of other materials due to its ability to be customized for exploration of fracture behavior including mixed-mode conditions. The general specimen geometry and loading configuration used in quasi-static studies from prior work in polymer fracture [26] is illustrated in Fig. 2, where R is the radius of the specimen, a is the crack length, β is the crack angle with respect to the horizontal axis of the specimen. The Cartesian crack tip coordinates are denoted by the x- and y-axes parallel and perpendicular to the crack, respectively. The corresponding crack tip polar coordinates r and θ are as shown.

For quasi-static implementation, the specimen is supported at two points along its lower edge while compressed along the vertical axis. As investigated in [25], the stress intensity factors at the crack tip, and therefore the mode mixity under quasi-static conditions, is controlled by the geometric parameters of the test setup namely, R, a, β, and the support span, S (for the quasi-static implementation only, hence not shown).

The proposed dynamic configuration (Fig. 2 (b)), on the other hand, has a single loading point, thus eliminating the experimental challenges associated with the two support points. The specimen is completely unsupported on its flat edge during loading event and is inertially loaded during the fracture event. This simplified loading configuration avoids issues with other experimental factors such as specimen alignment and support point friction detailed in [26]. Furthermore, it simplifies the loading configuration for complementary or supplementary numerical simulations including crack growth using force or displacement history measurements from the long bar. By varying the geometric parameters, R, a, and β, the geometry can achieve the complete range of mode mixities, to include combined conditions of crack sliding and crack opening. Moreover, even conditions of crack sliding with crack closing forces acting on the crack faces can be achieved in this geometry which is also of interest in many situations. The relationship between geometric parameters and mode mixity is dependent on material elastic and fracture properties. As is documented in the appendix, this flexibility of the geometry is convenient for the dynamic case as it allows the specimen to be configured as needed for a given material.

Further details regarding the test specimen geometry and loading configuration are shown in Fig. 3. The specimen is placed at the end of the incident bar. An adjustable micromechanical stage is used to hold the test specimen at the required height such that the

Table 1
Summary of digital image correlation parameters for dynamic fracture experiments.

Hardware Parameters		Analysis Parameters	
Camera Manufacturer	Kirana	Software	NCORR
Camera Model	05 M	Manufacturer	Open source
Image Resolution	924 × 768	Image Filtering	Guided filter
Lens Manufacturer	Nikkor	Sub-image Size	45 pixels radius
Focal Length	80–400 mm	Step Size	5 pixels
Field of View	50 mm × 50 mm		
Image Scale	16.7 pixels/mm		
Stereo Angle	N/A		
Image Acquisition Rate	500,000 fps		
Patterning Technique	Ink stamp		
Approximate Feature Size	5–7 pixels		

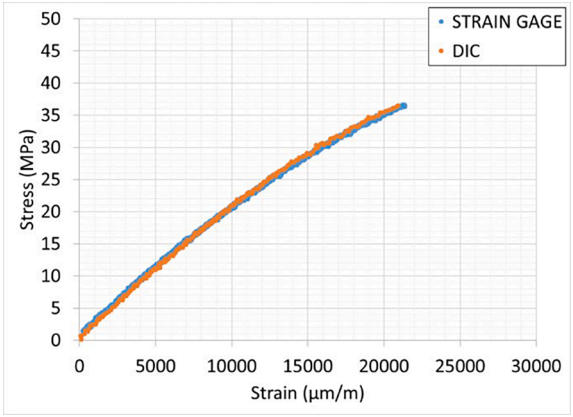

Fig. 5. Quasi-static tensile stress–strain response of the epoxy-based adhesive studied.

Table 2
Epoxy adhesive measured material properties.

Elastic modulus	2.2 GPa (±0.2 MPa)
Poisson's ratio	0.33
Density	1107 kg/m^3

centerline of the incident bar is aligned with the centerline of the specimen (annotated by $F(t)$ in Fig. 2 (b)). A strip of putty is used to hold the specimen in place on the stage and a second piece of putty is placed on the opposite edge of the specimen to minimize asymmetries with respect to acoustic impedance.

In typical long bar setups (e.g. split Hopkinson pressure bar), the second bar on the support side of the specimen is used to measure transmitted strain for dynamic loading of a fracture specimen. In those setups, the transmitted strain is used in conjunction with the incident strain to estimate the force history in the specimen necessary for extracting experimental quantities of interest in the test specimen. This often introduces uncertainties because estimation of force history is reliant on strain signal alignment (superposition) and appropriate assumptions about dispersion in elastic waves. Though rarely acknowledged, the former is non-trivial in the presence of noise in the signal. Utilizing this approach coupled with a full field method for extracting fracture parameters enables implementation of tests without the use of a second transmitter bar.

2.3. Specimen fabrication

Core shell rubber-toughened epoxy test specimens were fabricated for development and demonstration of the proposed experimental procedure. A set of aluminum molds (Fig. 4) was fabricated with semi-circular cavities of the desired in-plane dimensions (100 mm diameter). An epoxy formulation representative of a broad range of epoxy-based adhesive materials from the standpoint of elastic and failure properties was chosen for the present work. The selected epoxy formulation is a basic mix of difunctional bisphenol A/epichlorohydrin derived liquid epoxy resin (EPON^{TM} 828) with triethylenetetramine (EPIKURE^{TM} 3234) curing agent. Based on manufacturer recommendations, the two components were mixed at a ratio of 100:13 by weight. Prior to mixing, the EPON^{TM} 828 was heated to 66 °C. Core-shell rubber particles (PARALOID™ EXL-2691J) were then mixed in at a ratio of 10 % by weight using a Flaktek speedmixer. The speedmixer is a dual asymmetric centrifuge planetary mixer that reduces the opportunity for air entrapment in the mixer. After mixing, the mixture was allowed to cool to room temperature prior to adding the amine-based hardener and mixing it further. The epoxy mixture was then poured into the mold cavity. A sharp razor was inserted into the mold with the help of a template to align the razor blade to the desired inclination angle. A clip was attached to the razor blade to hold it in place while the epoxy cured. The samples were cured for approximately 18–24 h at room temperature followed by a post cure step for 2 h at 93 °C. The face of each test sample was then milled flat to the desired nominal thickness of 6.4 mm. The geometry of the crack tip is left as-cast. The cast-in-place razor blade forms a very repeatable crack with consistent lengths and consistent crack tip geometry with a root radius of the order 20 μm from sample to sample. It also minimizes the amount of post-cure machining and thus any local damage and residual stresses in the vicinity of the crack tip is avoided. The only machining operation required after curing is to machine the top face of the sample to the desired thickness. Photos of the finish-machined test sample and the crack are shown in Fig. 4.

2.4. Displacement field measurements

For the proposed set of experiments, a frame rate of 500,000 frames per second was chosen with acquisition beginning 250 micro-seconds after the striker bar contacts the incident bar. This time delay was determined based on the time required for the wave to propagate the length of the incident bar and into the specimen. For the 1.83 m aluminum incident bar, the elastic wave requires approximately 370 microseconds to propagate the bar's length. The time delay (250 micro-seconds), followed by the 360 micro-second time period of image acquisition (180 frames) allows adequate time to begin capturing images prior to loading followed by a series of images corresponding to the loading, crack initiation, and crack propagation phases in the specimen. The test specimen was positioned at a distance of 0.9 m from the focal plane of the camera resulting in the edges of the region of interest being located within 2° of the optical axis to minimize paraxial effects. The image correlation software, Ncorr [27], was used to perform the speckle image correlations on recorded images to quantify displacements in the two orthogonal in-plane directions. Based on the subset spacing (5 pixels), and the pixel scale factor (~0.06 mm), the resulting distance between neighboring output points was 0.36 mm. The parameters for the digital image correlation setup are summarized in Table 1.

2.5. Stress intensity factor extraction

Two separate methods were utilized for stress intensity factor extraction in the present work. The first approach is implemented through a hybrid DIC-FE methodology [26]. The general flow of the methodology is as follows: experimental displacement measurement, data filtering, mesh generation, output request definition, FE model execution, and data extraction. The experimentally measured displacement data is filtered using a guided edge filter (He, et al. [28]). This was chosen to minimize noise within the displacement data set while preserving specimen edges as well as higher variance regions, particularly along the crack faces. A custom-developed Matlab® script then utilizes the nodal position data to build a mesh that is coincident with the DIC grid points and derive the necessary element connectivity. Since the FE nodal positions are inherited from the DIC subset points, problems that arise due to spatial misalignment of the DIC subset points with the FE nodal coordinates are avoided. The FE mesh is updated for each image in the series of crack propagation images such that the FE nodal coordinates are always aligned to the DIC subset points. Once the nodal positions and element connectivity have been established, the script writes the node and element data into a text file in the Abaqus input file order and syntax. Lastly, the script also writes the material property definitions for the model, and the appropriate output requests are written to extract the fracture parameters of interest. The energy release rate is computed directly by the Abaqus structural solver using a domain (area) integral. The *J*-integral, as presented in Shih, et. al. [29], is defined as:

$$J = \int_A \left(-W\delta_{ij} + \sigma_{ij}\frac{\partial u_j}{\partial x_1} \right) \frac{\partial q_1}{\partial x_1} dA, (i,j = 1,2) \tag{1}$$

where A is the area of the domain or the area that includes the crack tip being evaluated and q_1 is a weighting function that equals 1 on the outer boundary of the domain and 0 on the inner boundary of the domain. The strain energy density is denoted as W, u is the displacement vector, and σ_{ij} is the stress tensor. The domain integral is then decomposed into the two stress intensity factors K_I and K_{II} for modes I and II, respectively, using the interaction integral technique described in [30] within the Abaqus solution process.

The second approach extracts fracture parameters from the experimentally measured displacements using an over-deterministic least-squares error minimization approach. Two separate sets of equations are utilized for this approach, one for preinitiation and one for post initiation. For the displacement field around the crack tip prior to crack initiation, the over-deterministic least-squares results are computed using the equations reported in [31] for the crack sliding (u_x) and crack opening displacements (u_y):

$$\begin{aligned} u_x = &\sum_{n=1}^{N} \frac{(K_I)_n}{2\mu} \frac{r^{\frac{n}{2}}}{\sqrt{2\pi}} \left\{ \kappa \cos\frac{n}{2}\theta - \frac{n}{2}\cos\left(\frac{n}{2}-2\right)\theta + \left\{\frac{n}{2} - (-1)^n\right\}\cos\frac{n}{2}\theta \right\} \\ &+ \sum_{n=1}^{N} \frac{(K_{II})_n}{2\mu} \frac{r^{\frac{n}{2}}}{\sqrt{2\pi}} \left\{ \kappa \sin\frac{n}{2}\theta - \frac{n}{2}\sin\left(\frac{n}{2}-2\right)\theta + \left\{\frac{n}{2} - (-1)^n\right\}\sin\frac{n}{2}\theta \right\} + T_X \end{aligned} \tag{2}$$

$$\begin{aligned} u_y = &\sum_{n=1}^{N} \frac{(K_I)_n}{2\mu} \frac{r^{\frac{n}{2}}}{\sqrt{2\pi}} \left\{ \kappa \sin\frac{n}{2}\theta + \frac{n}{2}\sin\left(\frac{n}{2}-2\right)\theta - \left\{\frac{n}{2} + (-1)^n\right\}\sin\frac{n}{2}\theta \right\} \\ &+ \sum_{n=1}^{N} \frac{(K_{II})_n}{2\mu} \frac{r^{\frac{n}{2}}}{\sqrt{2\pi}} \left\{ -\kappa \cos\frac{n}{2}\theta - \frac{n}{2}\cos\left(\frac{n}{2}-2\right)\theta + \left\{\frac{n}{2} - (-1)^n\right\}\cos\frac{n}{2}\theta \right\} + T_Y \end{aligned} \tag{3}$$

In the above equations, μ is the material shear modulus, and r and θ are the polar coordinates with crack tip as the origin and $\kappa = \frac{3-\upsilon}{1+\upsilon}$ for plane stress and υ is the Poisson's ratio. The coefficients K_I and K_{II}, when $n = 1$, are the mode I and mode II stress intensity factors. For digital image correlation experiments, the u_x and u_y fields are known for a set of points in the polar coordinates r and θ, as illustrated in Fig. 2.

By selecting a group of points in the vicinity of the crack, a set of linear equations can be formed to determine the $(K_I)_n$ and $(K_{II})_n$. Using an over-deterministic approach, the experimental crack opening displacement can be used for extracting mode I fracture components whereas the crack sliding displacements can be used for mode II fracture components. However, it has been shown that by transforming experimental in-plane Cartesian displacements into radial (u_r) and angular (u_θ) displacements, more accurate SIFs can be

Table 3
Rate dependence of elastic modulus derived from DSR method (values in italics are extrapolated, value in bold represents expected modulus for the present work).

Strain Rate (s^{-1})	Predicted Modulus (GPa)
$\sim 10^{-3}$	2.00
$\sim 10^{-2}$	2.04
$\sim 10^{-1}$	2.08
$\sim 10^{0}$	*2.13*
$\sim 10^{1}$	*2.17*
$\sim 10^{2}$	***2.21***
$\sim 10^{3}$	*2.25*
$\sim 10^{4}$	*2.29*

found in mixed-mode problems [18]. That is, the Cartesian displacement components can be transformed into polar components as shown in [4].

$$\begin{Bmatrix} u_r \\ u_\theta \end{Bmatrix} = \begin{bmatrix} \cos\theta & \sin\theta \\ -\sin\theta & \cos\theta \end{bmatrix} \begin{Bmatrix} u_x \\ u_y \end{Bmatrix} \tag{4}$$

where f and g are the functions from Equations [2] and [3] and T_x and T_y are terms representing rigid body motion. Experimental radial (u_r) displacement data was extracted for $0.5 \le r/B \le 1.5$ and $-120^{\circ} \le \theta \le 120^{\circ}$ for extraction of fracture parameters. The over-determined equation set with $n = 1$ was formed and solved for minimizing the least-squares error to compute values of K_I, K_{II}, T_x, and T_y for the crack up to the point of initiation.

Once the crack begins to propagate, the opening and sliding displacements can instead be written as:

$$\begin{aligned} u_x = &\sum_{n=1}^{N} \frac{(K_I)_n B_I(c)}{2\mu} \sqrt{\frac{2}{\pi}} (n+1) \left\{ r_1^{n/2} \cos\frac{n}{2}\theta_1 - h(n) r_2^{n/2} \cos\frac{n}{2}\theta_2 \right\} \\ &+ \sum_{n=1}^{N} \frac{(K_{II})_n B_{II}(c)}{2\mu} \sqrt{\frac{2}{\pi}} (n+1) \left\{ r_1^{n/2} \cos\frac{n}{2}\theta_1 - h(\bar{n}) r_2^{n/2} \cos\frac{n}{2}\theta_2 \right\} \end{aligned} \tag{5}$$

$$\begin{aligned} u_y = &\sum_{n=1}^{N} \frac{(K_I)_n B_I(c)}{2\mu} \sqrt{\frac{2}{\pi}} (n+1) \left\{ -\beta_1 r_1^{n/2} \sin\frac{n}{2}\theta_1 - \frac{h(n)}{\beta_2} r_2^{n/2} \sin\frac{n}{2}\theta_2 \right\} \\ &+ \sum_{n=1}^{N} \frac{(K_{II})_n B_{II}(c)}{2\mu} \sqrt{\frac{2}{\pi}} (n+1) \left\{ \beta_1 r_1^{n/2} \cos\frac{n}{2}\theta_1 + \frac{h(\bar{n})}{\beta_2} r_2^{n/2} \cos\frac{n}{2}\theta_2 \right\} \end{aligned} \tag{6}$$

In the above equations, μ is the material shear modulus, and r and θ are the polar coordinates with crack tip as the origin and $\kappa = \frac{3-\upsilon}{1+\upsilon}$ for plane stress. The longitudinal and shear wave speeds are defined as $C_L = \sqrt{\frac{(\kappa+1)\mu}{(\kappa-1)\rho}}$ and $C_S = \sqrt{\frac{\mu}{\rho}}$ respectively. The non-dimensional quantities, $\beta_1 = \sqrt{1 - \left(\frac{c}{C_L}\right)^2}$ and $\beta_2 = \sqrt{1 - \left(\frac{c}{C_S}\right)^2}$ are used to compute the spatial variations of $r_m = \sqrt{X^2 + \beta_m^2 Y^2}$ and $\theta_m = \tan^{-1}\left(\frac{\beta_m Y}{X}\right)$ based on the crack speed, c. Also, B_I, B_{II}, D, and h are defined in [7] as,

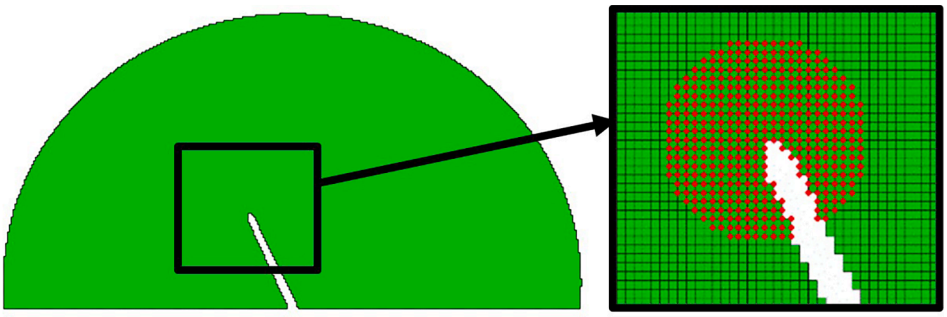

Fig. 6. Example of points considered in domain integral calculation (green squares are FE model elements, red-highlighted points are nodes included in contour integral evaluation). (For interpretation of the references to colour in this figure legend, the reader is referred to the web version of this article.)

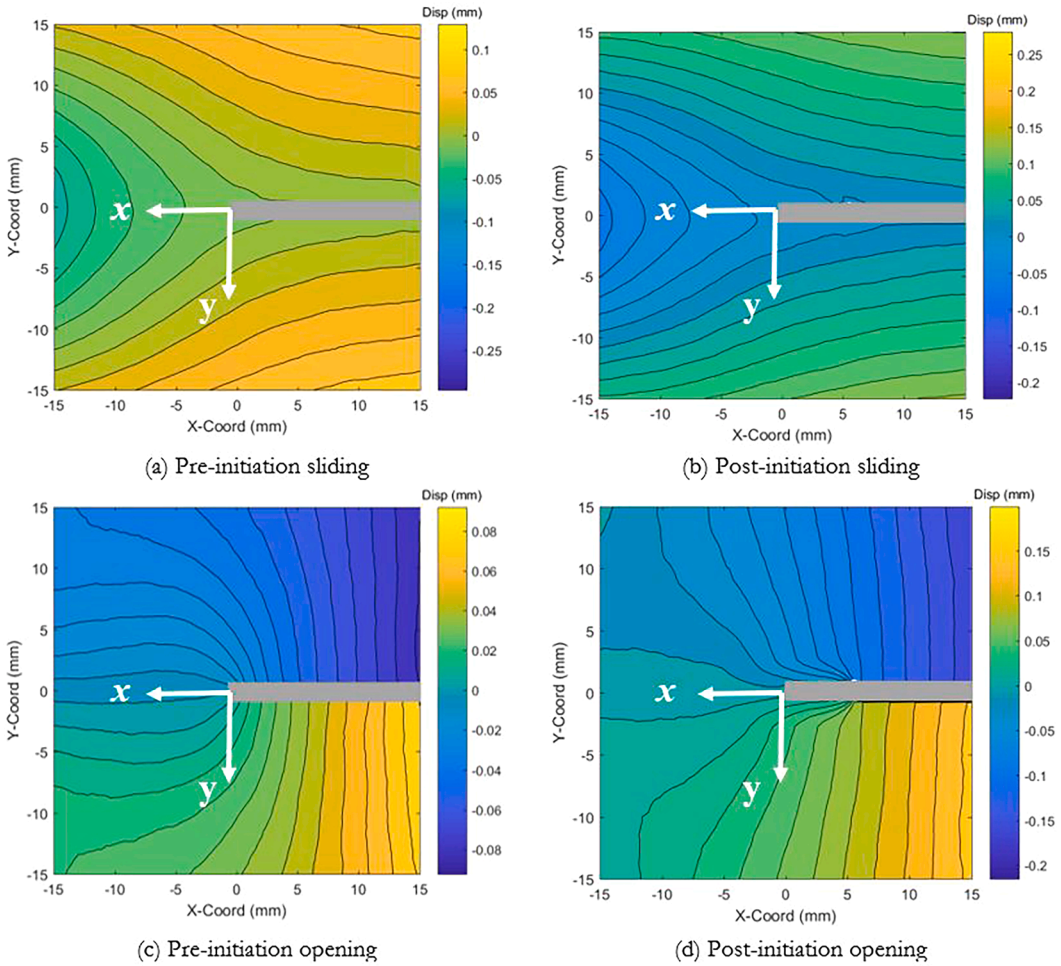

Fig. 7. Displacement plots for β = 90° experiment (Pre-initiation displacements from ~ -4 μs and post-initiation displacements from ~ 20 μs; t = 0 corresponds to crack initiation).

$$B_I(c) = \frac{\left(1+\beta_2^2\right)}{D},\ B_{II}(c) = \frac{2\beta_2}{D}$$

$$D = 4\beta_1\beta_2 - \left(1+\beta_2^2\right)^2$$

$$h(n) = \begin{cases} \dfrac{2\beta_1\beta_2}{1+\beta_2^2} & \text{for even n} \\ \dfrac{1+\beta_2^2}{2} & \text{for odd n} \end{cases}$$

$$h(\bar{n}) = h(n+1), \bar{n} = n+1 \tag{7}$$

For both methods of extracting stress intensity factors, it is important to understand the location of the crack tip. For the present work, the location is identified manually from the DIC images. A local crack coordinate system that realigns with the instantaneous crack propagation direction is used. The SIF values extracted using the domain integral method is much less sensitive to the accuracy of the crack tip location. This sensitivity is documented in [26].

2.6. Uniaxial material behavior

2.6.1. Quasi-static testing

To acquire the elastic properties of the baseline material, tension tests were conducted with ASTM D 638 [32] and ASTM D 695 [33] as guidelines. Several tension and compression specimens were cast and cured. The uniaxial tests were conducted on a Tinius Olsen

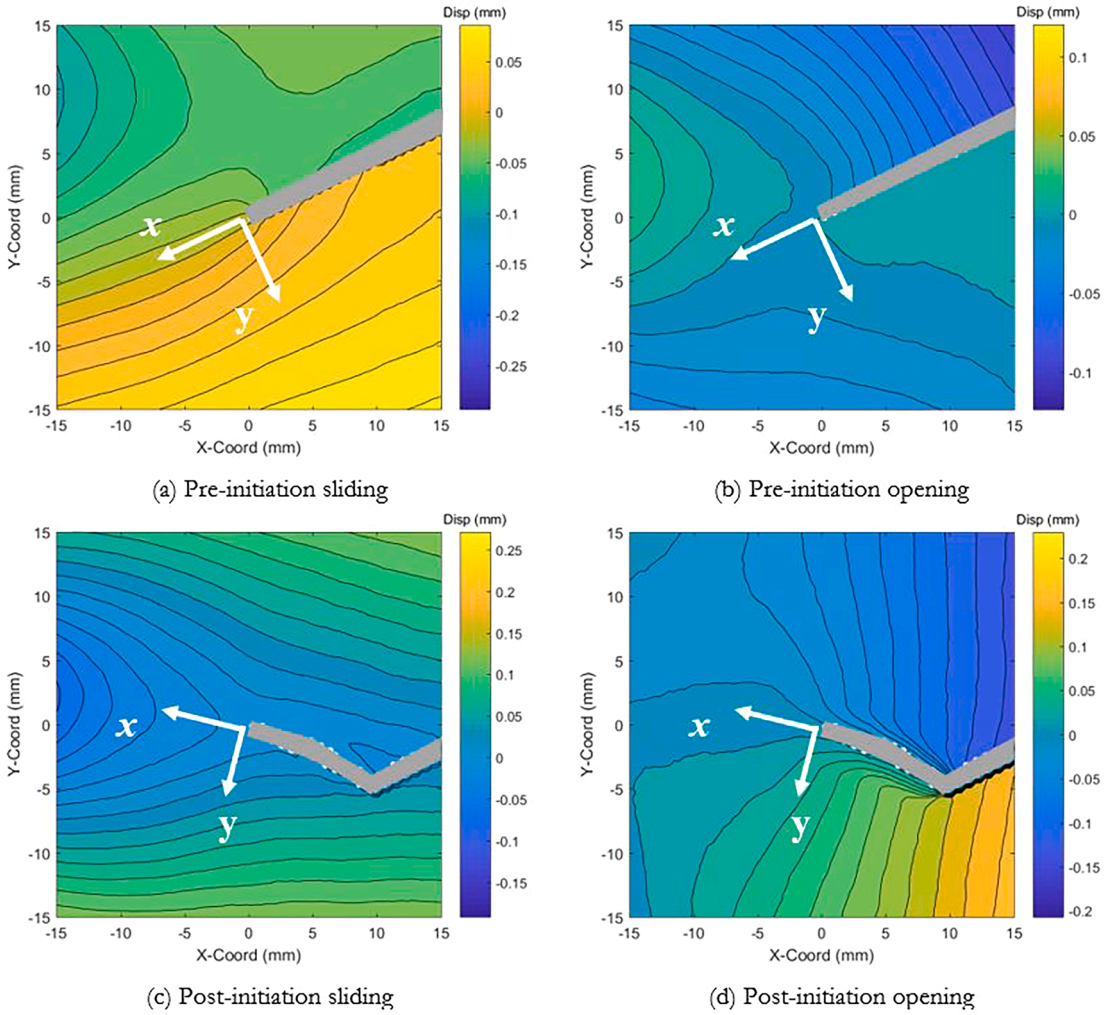

Fig. 8. Displacement plots for $\beta = 65^{\circ}$ experiment (Pre-initiation displacements from $\sim$ -4 μs and post-initiation displacements from $\sim$ 24 μs; t = 0 corresponds to crack initiation).

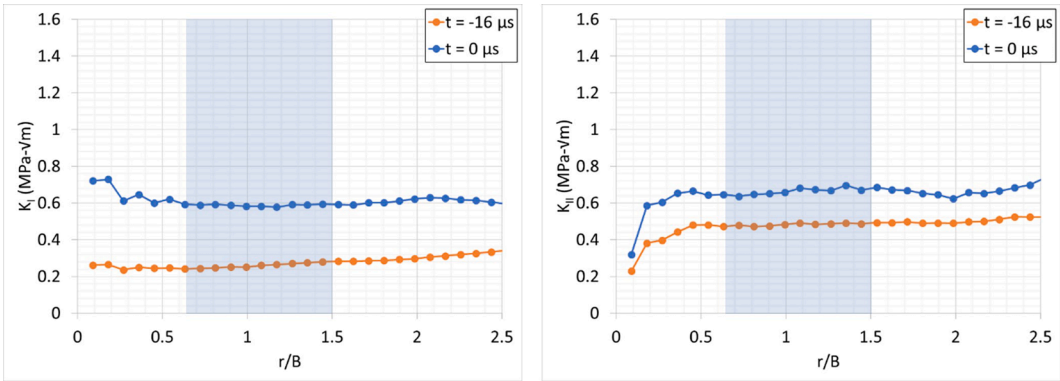

Fig. 9. Dependence of stress intensity factors on the extent of the domain of integration for pure mode I test (upper) and near mode II test (lower).

uniaxial load test frame. The specimens were loaded under displacement control at a rate of 0.25 mm/min. A 44.5 kN capacity load cell (accuracy = 0.04 % of full scale) was used to measure the applied load. The tensile stress vs strain data for the material is shown in Fig. 5 with comparisons between the response measured using a strain gage to that as extracted using strains derived from digital image

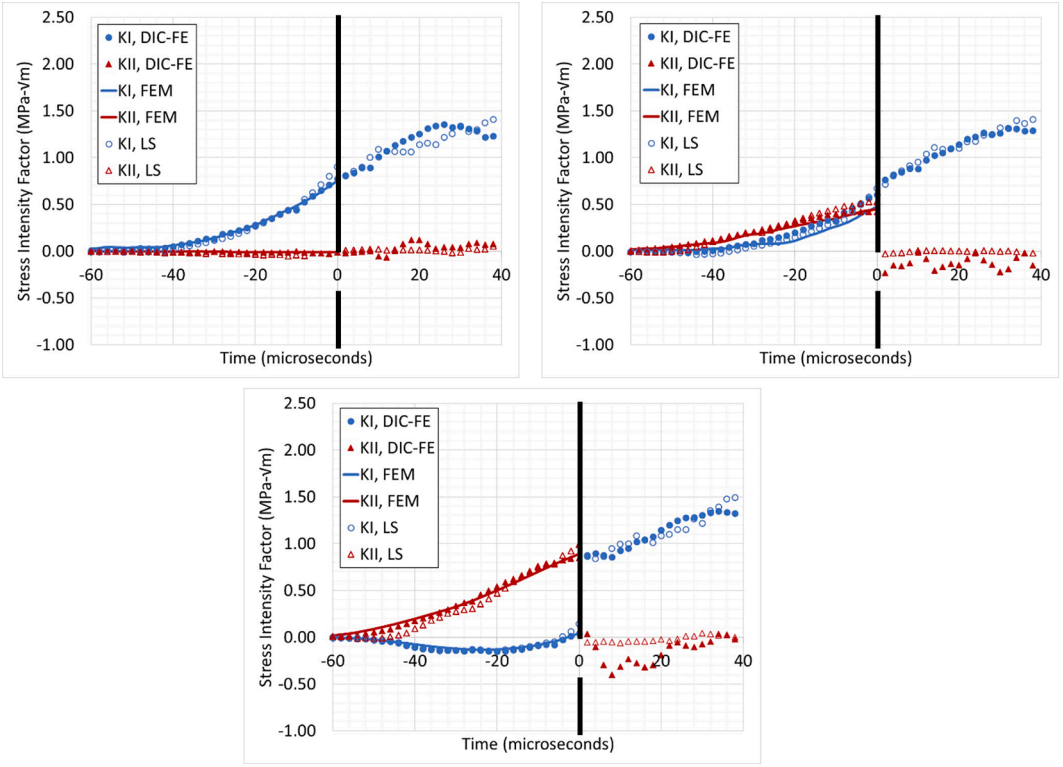

Fig. 10. Stress intensity factor histories for three different crack inclination angles: Pure mode I – $\beta = 90^{\circ}$ (top), mixed mode – $\beta = 80^{\circ}$ (center), and Pure mode II – $\beta = 65^{\circ}$ (bottom).

correlation displacement data.

The elastic modulus for the linear model was calculated as the average slope across the range of 2000 to 4000 microstrain. The material properties of this epoxy formulation are summarized in Table 2.

2.6.2. Dynamic testing

In the fracture parameter extraction process it is assumed that the material behavior is linear elastic. Since this testing occurs under elevated strain rates, this assumption was verified using dynamic mechanical analysis and the DSR method [34]. This technique has been demonstrated to work well across a range of strain rates for PMMA and polycarbonate in [34] as well as EPON 826 in [35] by comparing predicted response to measured responses at different rates using split Hopkinson pressure bar testing. By measuring the loss modulus at multiple frequencies (1 Hz, 10 Hz, and 100 Hz in the present work), it was determined that the α-transition point (which is most relevant to the current work) shifts at a rate of approximately 5 °C per decade of increase in frequency or strain rate.

Based on these results, the material's elastic modulus is expected to have some rate dependence, particularly at higher and lower temperatures where the material may be operating near one of its transition points. The predicted elastic modulus at a range of strain rates is tabulated in Table 3. The strain rates calculated from complementary dynamic FE models for the present work (see Appendix) are on the order of 10^2 s^{-1}. Considering dynamic fracture testing at room temperature, the rate-dependent elastic effects are expected to be small with the modulus being expected to shift less than 5 % across the strain rates of interest in the current geometry and under the current impact conditions, thus justifying a linear elastic material model assumption for the hybrid DIC-FE data extraction process. This variation in modulus is consistent with observations from data presented in [34] for an epoxy-based material with a very similar composition.

3. Critical examination of initial fracture experiments

An initial set of tests was conducted with the proposed geometry with a striker velocity of 8 m/s. The choice was based on parametric studies, documented in the appendix, to identify appropriate impact conditions to achieve the desired strain rate and range of mode mixities. For each test, the striker velocity, incident bar strain, and specimen images were all recorded. The primary objective of the first set of experiments was to quantify any variations with respect to contour path dependence and compare the fracture quantity extraction methods. Using the hybrid DIC-FE approach, the domain integral quantities were extracted from the model. For

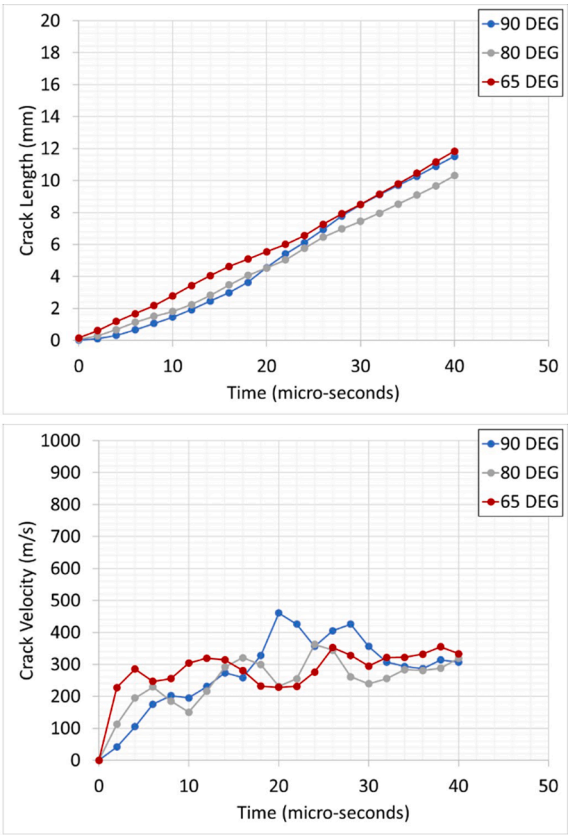

Fig. 11. Crack tip position history (top) and crack tip velocity (bottom) for pure mode I ($\beta = 90°$), mixed mode ($\beta = 80°$), and pure mode II ($\beta = 65°$).

reference, the mesh in the post-processing model is inherited directly from the DIC output data. Therefore, each node in the post-processing model utilizes the same displacement values from its associated DIC output data point. By default, Abaqus performs the contour integral computation for individual sets of elements that enclose the crack tip. To assess path dependence, successive contours must be extracted at increasing radial extents from the crack tip. In the present work, circular contours of elements were manually specified around the crack tip as illustrated in Fig. 6.

Displacement contours were plotted to visualize and understand the evolution of the elastic deformation in the vicinity of the crack tip. For example, the sliding and opening displacements for a mode I crack are shown in Fig. 7. As evidenced in the figure, the opening displacement field is quite symmetric implying a mode I dominant deformation at the point of initiation that persists well into the crack propagation event.

The example displacements of the pure mode II case is shown in Fig. 8. In these contour plots for $\beta = 65°$, the displacement fields are asymmetric and dominated by sliding displacement at initiation. Early in the propagation event, the deformation pattern quickly approaches a symmetric opening displacement field relative to the growing crack tip (or local rotated) coordinates as would be expected for a pure mode I crack.

The stress intensity factor output is plotted as a function of the ratio of r/B for the pure mode I and near mode II case in Fig. 9, where r is the radial distance from the crack tip and B is the specimen thickness. For reference, a value of $r/B = 1$ corresponds to a contour radius of 6.37 mm from the crack tip.

For each of these scenarios, one set of contour outputs is plotted for a time close to crack initiation ($t \approx 0$ μs) and another set of contour integral outputs is plotted for a time earlier in the loading event, approximately halfway to crack initiation. As shown in the figure, the stress intensity factors are relatively invariant of contour location at each of the time steps inspected.

The stress intensity factor histories for three different mode states are plotted in Fig. 10. Prior to crack initiation (which corresponds to $t = 0$ μs in the plot) the predicted SIF histories from complementary elasto-dynamic finite element simulations (see Appendix for details) are compared with the experimentally derived SIF histories as extracted using the two methods discussed in earlier sections, namely the over-deterministic, least squares (LS) approach and the hybrid DIC-FE approach. The simulated results show excellent agreement with the experimental values. For $\beta = 80°$ crack inclination angle, the values from the finite element simulation are slightly lower than those that are experimentally measured using the hybrid DIC-FE data reduction method for both mode I and mode II. The pre-initiation values extracted using the least squares method show a slightly larger deviation from the FE simulation results and the values extracted using the DIC-FE method; however, this deviation is still very low throughout the time history preceding initiation.

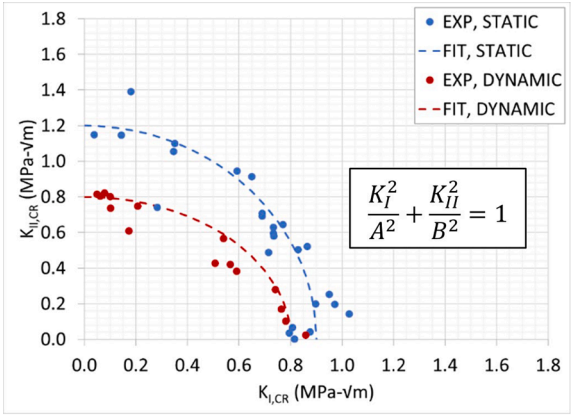

(a)

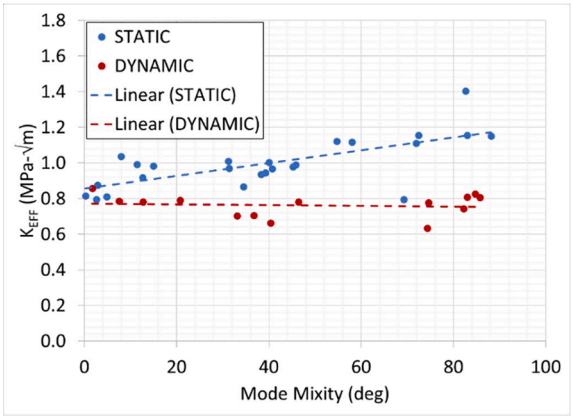

(b)

Fig. 12. (a) Fracture envelopes from measured critical stress intensity factors for static and dynamic experiments and (b) relationship between effective critical stress intensity factor and mode mixity.

Table 4
Stress intensity factor envelope fit parameters.

Condition	Curve Fit Parameter (MPa-$\sqrt{m}$)	
	A	B
Static	0.9	1.2
Dynamic	0.8	0.8

The post-initiation stress intensity factor histories ($t > 0$ μs) are computed using the hybrid DIC-FE approach and compared with the ones obtained using over-deterministic least squares approach. In the post-initiation phase, the data from dynamic finite element model is not available since no attempt to simulate crack growth was made in the present work. However, the least squares calculations match well with the hybrid DIC-FE results. For the two experiments that have a dominant mode I component ($\beta = 90^\circ$ and 80° crack angle cases), the slope of the mode I SIF component undergoes very little change between the pre- and post-initiation states. This implies that the initial crack is likely very sharp geometrically. For all three of the experiments, the mode I stress intensity factor plateaus at approximately 1.4 MPa-$\sqrt{m}$. In general, for the latter two cases, the mode II stress intensity factor rapidly decreases to near zero soon after initiation and approaches zero as the crack approaches a mode I dominant state during propagation. Post-initiation, the mode I component of the least squares results appear to have more noise. This is likely due to uncertainties with respect to crack tip location, as that influences the displacement values used to form the over-determined equations in the asymptotic expansion. Conversely, the mode II component of the results extracted using the DIC-FE method appear to have more noise. While this method has been shown [26] to be relatively insensitive to the selection of the crack tip location, uncertainties in manually orienting the local crack tip coordinates may still contribute to deviations in this measurement.

For each of the dynamic experiments, the crack tip position is manually tracked as a function of time by manually inspecting the raw images of the test sample and separately inspecting the displacement field contours. The crack tip positions are plotted as a

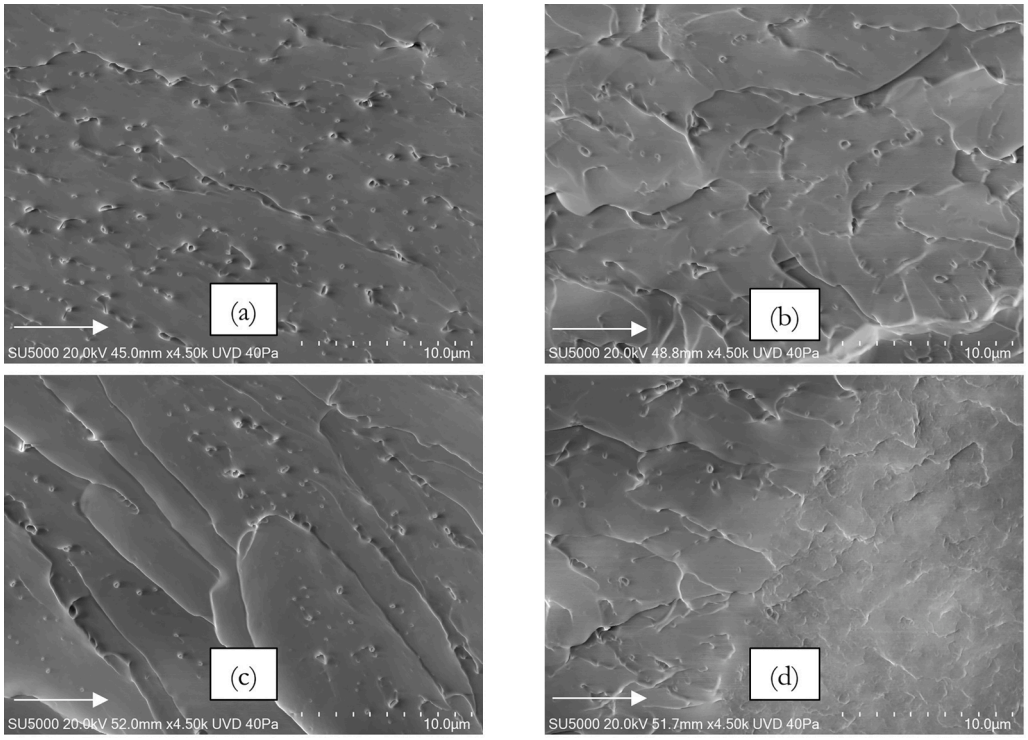

Fig. 13. Micrographs comparing fracture surfaces from (a) quasi-static mode I, (b) dynamic mode I, (c) quasi-static mode II, (d) dynamic mode II (arrow indicates propagation direction).

function of time in Fig. 11 for $\beta = 90°$, 80°, and 65° cases. The mode I ($\beta = 90°$) and mode II ($\beta = 65°$) test specimens have near-identical displacement histories, whereas the mixed-mode case ($\beta = 80°$) still follows a similar trend.

The crack tip velocity for each of the cases was estimated using numerical differentiation of the displacement histories and is plotted in Fig. 11. Prior to differentiation, the crack tip position values were smoothed using a Bezier fit (cubic curve with smoothing parameter of 0.5) as has been utilized by previous authors [36]. The velocity is relatively consistent between the three different crack inclination angles. Considering velocity values in the range of 15 to 40 μs after crack initiation, the average velocity was estimated to be 312 m/s with a standard deviation of 56 m/s.

4. Results and discussion

4.1. Mixed-mode fracture envelope

With the proposed experimental setup, a test series was executed for a range of crack inclination angles from $\beta = 65°$ to 90° to develop an understanding of the critical stress intensity factors at crack initiation across the full range of mode mixities under stress wave loading conditions. For each test case, the results were extracted using the DIC-FE method and are plotted in Fig. 12. For comparison, the results from quasi-static experiments from the authors' earlier work on the same adhesive material [26] are shown as well.

The parameters for the fit are summarized in Table 4. An alternate representation of the mixed-mode fracture behavior of this adhesive is shown in Fig. 12 (b). Here, the effective stress intensity factors at crack initiation $\left(K_{eff} = \sqrt{K_I^2 + K_{II}^2}\right)$ under static and dynamic loading conditions are plotted as a function of mode mixity by the red solid symbols. Again, for comparison, the quasi-static counterparts are shown for the same adhesive material by the blue solid symbols. A linear fit is also shown on the plot for both sets of data. Under dynamic conditions, the critical effective stress intensity factors are relatively constant within the experimental scatter with respect to mode mixity. On the contrary, for the quasi-static experiments, a perceivable increasing trend in the critical effective stress intensity factors with mode mixity (or, increasing critical mode II values) is evident. Approximately 38 % higher value of critical K_{eff} under mode II conditions relative to the pure mode I value can be estimated from the plot. It should be noted that the relationship between effective stress intensity factor and mode mixity is considered a material dependent characteristic. For instance, Lim, et. al. [37] observed a general decrease in effective stress intensity factor with increasing mode mixity for soft rocks. Miller [38] observed a similar decreasing trend for a rubbery particulate composite. In a study of mixed-mode fracture in epoxy, however, Jamali et al. [39] observed an increase in strain energy release rate of approximately 2.47X across the range of mode mixities from pure mode I to pure

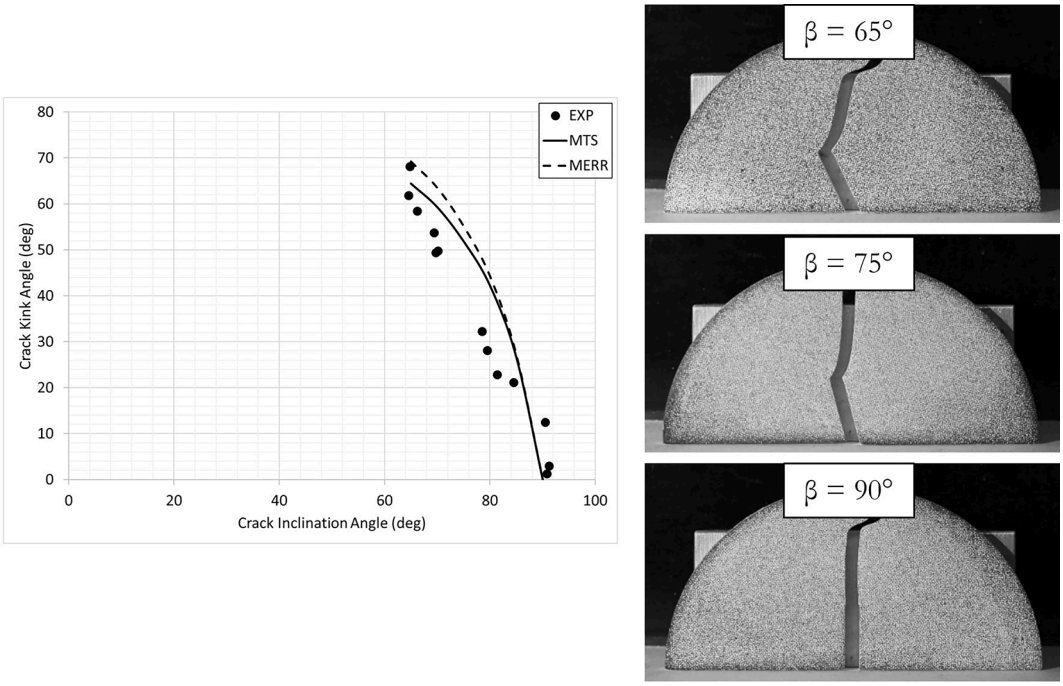

Fig. 14. Comparison of crack propagation direction with predictions using MTS and MERR criteria.

mode II and noted similar trends in other epoxies.

Interestingly, the dynamic results were measurably lower than the static counterparts for this adhesive, with a larger change in the two sets of data occurring in the shear-dominated regime, close to the pure mode II case. Extensive uniaxial tension and compression testing, as well as torsion testing, revealed that the material exhibits an elastic-brittle response in tension, whereas, in compression and shear, it exhibits greater ability to deform inelastically. The inelastic behavior in polymers has been shown to be significantly affected by loading rate and that is suspected to be the case here since the tension-dominated fracture properties were measurably less rate-sensitive. Several prior works have observed a similar effect with respect to differences between quasi-static and dynamic fracture toughness. Most recently, mode I fracture testing by Kanchanomai, et al. [40] measured a decrease in critical stress intensity factors with increases in loading rate. Work by Kalthoff, et al. [41] reported results from dynamic experiments where the initial dynamic stress intensity factor (at crack initiation) was lower than its static counterpart. However, dynamic values from later in the propagation were higher than their static counterparts. Marur, et al. [42] performed tests on particulate composites comprised of epoxy and alumina nanoparticles. Their results also demonstrated lower fracture toughness in dynamic conditions relative to their quasi-static counterparts for studies involving two different particle sizes and multiple volume fractions. Joudon, et al. [43] reported dynamic stress intensity factor values that were 88–91 % of their static equivalent for a neat epoxy material. Pittman and colleagues [44] studied mode I stress intensity factors for two different epoxy systems. One system, PR-520, exhibited static critical SIF values that were higher than the dynamic SIF values, whereas the other system, 3502, exhibited dynamic critical SIF values that were lower than the dynamic SIF values. All these works seem to support the observed rate dependent behavior of fracture envelopes.

4.2. *Fracture surface microscopy*

Fractography was also undertaken to shed light on potential differences in microscale failure mechanisms for the adhesive under different loading rates. Fracture surface (x-z plane) micrographs from tension- and shear-dominated fracture events are presented in Fig. 13 at a distance of $\frac{r}{B} = 1$ from the original crack front.

Evidently, the fractographs for quasi-static and dynamic mode I and mode II cases show visible differences. The dynamically loaded specimens appear to have fewer finer features relative to the quasi-static cases over the fractured surface. In the mode I case, numerous locations where crack pinning has occurred are clearly visible whereas the same are less dominant and mostly interspersed amongst broad, randomly cleaved features in the dynamic counterpart. Particle cavitation is another potentially significant mechanism dominant under quasi-static conditions appearing as pronounced localized features in contrast to the dynamic surface features. In the mode II case, the fracture surface features are again visibly dominant under quasi-static conditions relative to the dynamic counterparts. The crack has numerous pinned and cavitated locations besides cleaved structures. The same features are relatively muted under dynamic conditions. These textural differences are consistent with the lower critical stress intensity factor values at initiation for the dynamic case.

4.3. Crack propagation directions

For each test specimen, image analysis was used to measure the crack initiation direction as precisely as possible. For the full range of mode mixities, the expected crack propagation angles were first calculated using maximum tangential stress (MTS) criterion. This criterion states that the crack is assumed to crack grow when the maximum average tangential stress in the region ahead of the crack tip reaches its critical value and the crack growth direction corresponds to the direction of the maximum tangential stress along a constant radius around the crack tip. Higher order terms in Williams' asymptotic stress fields are considered to be negligible. Separately, the maximum energy release rate criterion was used to estimate expected crack propagation direction which postulates that the parent crack initially propagates in the direction that maximizes the value of energy release rate G or J. The estimated crack propagation directions are compared with the different criteria in Fig. 14. Given the difficulties in the measurement of crack kink angles from the initial crack tip, reasonably good agreement between the experimental results and those predicted by the two crack propagation direction criteria is evident.

5. Concluding remarks

Dynamic mixed-mode fracture behavior of an epoxy-based adhesive is studied experimentally. The work successfully demonstrates the adoption of an SCB three-point geometry to a simplified, single-point impact configuration to generate the full range of mixities (and beyond) for high strain rate fracture characterization. The digital image correlation method coupled with ultrahigh-speed photography was employed to measure in-plane deformations near cracks. A data reduction technique was investigated for extracting dynamic fracture parameters by utilizing the displacement measurements mapped into a finite element discretization. The data reduction approach was implemented using the Abaqus structural solver, allowing extraction of mode I and mode II stress intensity factors. Viscoelastic measurements were performed on the material of interest and the so-called decompose, shift, reconstruct method was used to predict the rate dependence of the elastic modulus to verify the use of a linear elastic material model for the data post-processing. The results indicated that for this rubber-filled epoxy adhesive there is minimal change in the elastic properties across the loading regime in this study. The dynamic fracture experimental setup was used to perform multiple experiments across a range of crack inclinations to obtain critical stress intensity factors over the full range of mode mixities. The results were compared with their quasi-static counterparts; for the mode II condition, the dynamic measurements were approximately 70 % of the quasi-static counterparts. This was also reflected in plots of the effective stress intensity factors as a function of mode mixity. For the dynamic tests, the effective stress intensity factors were relatively constant with mode mixity, whereas for the quasi-static case, the values increased approximately 38 % across the full range of mode mixities. Texture and feature differences noted in micrographs of quasi-static and dynamic specimen fracture surfaces are consistent with the differences between critical stress intensity factors at the two load states, particularly for the mode I case. Measured crack kink angles were compared to those predicted by popular crack propagation direction criteria.

CRediT authorship contribution statement

A. Taylor Owens: Methodology, Validation, Formal analysis, Data curation, Writing – original draft. **Hareesh V. Tippur:** Conceptualization, Methodology, Writing – review & editing.

Declaration of Competing Interest

The authors declare that they have no known competing financial interests or personal relationships that could have appeared to influence the work reported in this paper.

Data availability

The authors are unable or have chosen not to specify which data has been used.

Acknowledgements

Support for this work has been partially provided by the US Government. The support of Mr. Sean Thompson and Ms. Chappell Alex (US Army Development Command) to collect the SEM images is gratefully acknowledged.

Appendix A. Specimen and experimental design

A complementary dynamic model of the experimental setup was created in the Abaqus finite element modeling software to determine the effect of certain experimental parameters such as the crack length and crack angle on certain output quantities such as mode mixity and demonstrate the overall utility of this experimental setup. Two options were considered for introducing the experimentally derived force history into the test specimen. The first option is to estimate the force history using the incident and reflected strain signals in the incident bar (Fig. A1) and apply the force history directly to the specimen. The second option is to model the aluminum striker bar and incident bar with contact at the incident to striker interface and striker to specimen interface.

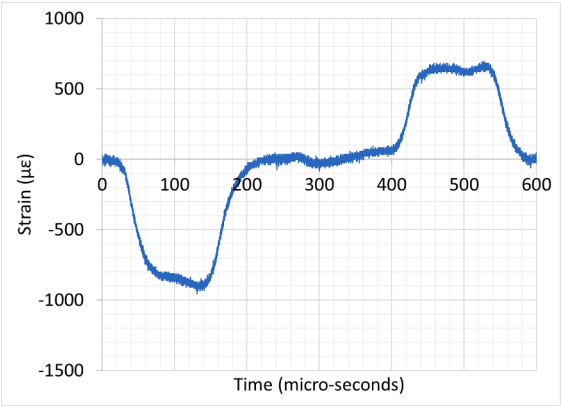

Fig. A1. Incident and reflected strain history measured from incident bar.

Each of the two approaches have advantages and disadvantages. As evident in Fig. A1, the incident and reflected signals must be aligned which is a nontrivial step and can result in uncertainty depending on the method chosen for signal alignment. In addition, considering the signal is measured at some distance away from the specimen uncertainty due to wave dispersion, though small in this work, could be a factor as well. These uncertainties are typically addressed in traditional two bar setups by using the one-dimensional equations of motion at the specimen faces to assess the estimated input force using the incident, reflected, and transmitted signals. The limitation with the second approach is uncertainty associated with the contact descriptions at the two interfaces. The second approach is also more computationally intensive but reliable. In the absence of a transmitter bar in the present work to estimate force balance, the second approach was chosen.

For the model, the test specimen was modeled using approximately 2,200 solid 4-noded reduced integration elements (S4R) with approximately 2,200 nodes. An elastic modulus of 2.2 GPa and a density of 1.11 g/cc was used for the epoxy specimen. An elastic modulus of 69 GPa and a density of 2.8 g/cc was used for the aluminum striker and long bar. An initial velocity was prescribed for the striker bar and contact was modeled at the interface between the striker bar and the long bar as well as between the long bar and the test specimen using the surface-to-surface contact algorithm in Abaqus. A study of friction at the interfaces showed that friction at these two interfaces had negligible effect on stress intensity factors. The interfaces were thus assumed to be frictionless. The automatic time stepping scheme was utilized in the model. To initially evaluate the performance of the model, a strain gage was mounted on the incident bar to verify that the stress wave loading was being captured appropriately. The strain data measured from the initial tests was in good agreement with that predicted in the finite element model with the strain averaged over a similar length segment in the model.

The mode mixity at failure is dependent upon the critical effective stress intensity factor for a given sample material and geometry (crack length and crack inclination angle). For the finite element-based parametric studies, an effective critical stress intensity factor, K_{eff}, of 0.7 MPa-$\sqrt{}$m was assumed for computing mode mixity at crack initiation where $K_{eff} = \sqrt{K_I^2 + K_{II}^2}$. This value was based on initial mode I dominated dynamic experiments.

A.1 Influence of crack length

Three crack lengths, 16 mm, 19 mm, and 22 mm, were analyzed with an impact velocity of 8 m/s. As shown in Fig. A2, the mode mixity at presumed crack initiation for the specimen with the shorter crack length is less sensitive to changes in crack inclination angle and thus, even at very shallow crack angles (β below 65° from the horizontal), pure mode II does not appear to be possible at the imposed velocity.

The longer cracks (19 mm and 22 mm), however, approach pure mode II at angles of 65° and 70° from the horizontal respectively. Based on these results, for a given material system with a given fracture toughness, it appears that crack length can be a useful experimental variable for sizing the specimen geometry to achieve a desired range of mode mixities. It is also interesting that at longer crack lengths, the crack inclination angle has a more significant influence on mode mixity at crack initiation (e.g., small changes in crack inclination angle lead to large changes in mode mixity). This may be undesirable from an implementation standpoint if, for instance, results are targeted for a specific mode mixity. Therefore, the crack length can be used to control that sensitivity.

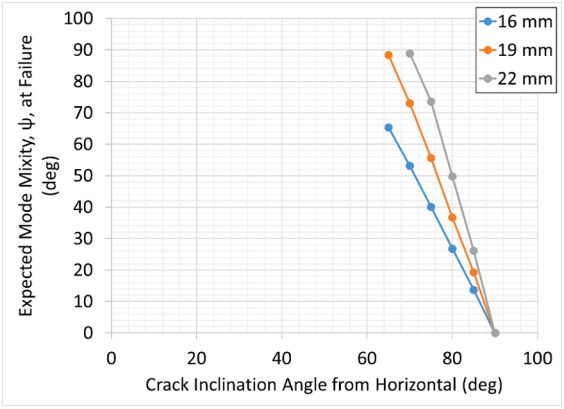

Fig. A2. Predicted mode mixity values for different crack angles for three different crack lengths.

A.2 Influence of striker velocity

With the 19 mm crack length, a series of analyses were executed to understand the influence of striker initial velocity on the apparent mode mixity at crack initiation. As shown in Fig. A3, as the striker velocity increases, the apparent mode mixity at crack initiation becomes more sensitive to changes in crack inclination angle.

Thus, for high striker velocities, very small changes in crack inclination angle are expected to result in very large changes in mode mixity at failure for a given material. Again, this may also be undesirable from an implementation standpoint. Likewise, for slower striker velocities, the experimental setup may not be able to achieve pure mode II conditions. For this combination of geometric parameters, a velocity of 8 m/s allows a sufficiently wide range of crack inclination angles to be tested to achieve the desired range of mode mixities. At lower velocities, the full range of mode mixities is less likely to be achieved, and for higher impact velocities, small changes in inclination angle result in large changes in mode mixity. This linear, dynamic finite element model demonstrates the flexibility of the experimental setup to enable study of fracture at a wide range of strain rates.

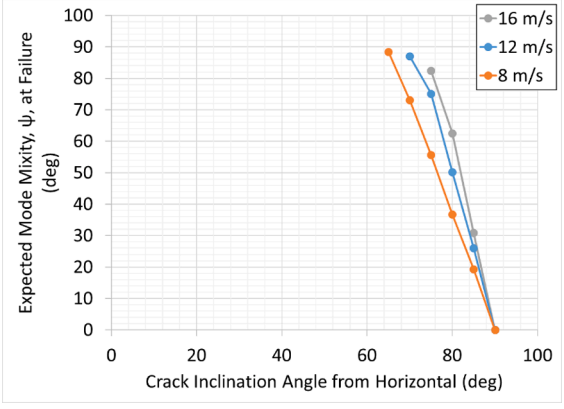

Fig. A3. Predicted mode mixity values for different crack angles for different striker velocities for crack length of 19 mm.

A.2 Influence of supports

In the present work, a strip of putty was used to hold the specimen in place while in contact with the incident bar. A second piece of putty was utilized on the opposite edge in the event of asymmetries in the boundary of the specimen resulting in asymmetric wave reflections. The complementary FE model was used to investigate the effects of the putty. Four different specimen edge boundary conditions were investigated: free-free, putty on one edge only, putty on both edges, and putty on both edges but with one piece of putty fixed. The results show that for pure mode I case ($\beta = 90°$), introduction of the putty on only one edge results in a slight asymmetry in the loading behavior, and hence a slight mode mixity ($<1°$). The model was also used to investigate the effect of the modulus of the support point, or more importantly, the impedance mismatch between the test specimen and the support point. As long as the acoustic impedance of the supporting material is substantially lower than the test specimen material and the contact area is minimum, as is the case for the epoxy being tested here, the effect is negligible.

References

[1] Ravi-Chandar K, Knauss WG. An experimental investigation into dynamic fracture: I. Crack initiation and arrest. Int J Fract 1984;25(4):247–62.
[2] Mason JJ, Lambros J, Rosakis AJ. The use of a coherent gradient sensor in dynamic mixed-mode fracture mechanics experiments. J Mech Phys Solids 1992;40(3):641–61.
[3] Nakano M, Kishida K, Ymauchi Y, Sogabe Y. Dynamic fracture initiation in brittle materials under combined mode I/II loading. J Physique IV Colloque 1994;04(C8):695–700.
[4] Gao G, Huang S, Xia K, Li Z. Application of digital image correlation (DIC) in dynamic notched semi-circular bend (NCSB) tests. Exp Mech 2015;55:95–104.
[5] Kinloch AJ, Shaw SJ, Tod DA, Hunston DL. Deformation and fracture behaviour of a rubber-toughened epoxy: 1. Microstructure and fracture studies. Polymer 1983;24:1341–54.
[6] Kinloch AJ, Shaw SJ, Hunston DL. Deformation and fracture behaviour of a rubber-toughened epoxy: 2. Failure criteria. Polymer 1983;24:1355–63.
[7] Pearson RA, Yee AF. Influence of particle size and particle size distribution on toughening mechanisms in rubber-modified epoxies. J Mater Sci 1991;26:3828–44.
[8] Bagheri R, Marouf BT, Pearson RA. Rubber-toughened epoxies: a critical review. J Macromol Sci, Part C: Polym Rev 2009;49(3):201–25.
[9] Peters W, Ranson W. Digital imaging techniques in experimental stress analysis. Opt Engng 1982;21(3):427–32.
[10] Sutton MA, Wolters WJ, Peters WJ, Peters WH, Ranson WF, McNeill SR. Determination of displacements using an improved digital correlation method. Image Vis Comput 1983;1(3):133–9.
[11] Peters WH, Ranson WF, Sutton MA, Chu T, Anderson J. Applications of digital correlation methods to rigid body mechanics. Opt Eng 1983;22(6):738–42.
[12] Chu TC, Ranson MA, Sutton MA. Applications of digital-image-correlation techniques to experimental mechanics. Exp Mech 1985;25(3):232–44.
[13] Schreier H, Orteu J-J, Sutton MA. Image Correlation for Shape, Motion and Deformation Measurements, New York. NY: Springer; 2009.
[14] Sanford RJ. Application of the least-squares method to photoelastic analysis. Exp Mech 1980;20:192–7.
[15] Sanford RJ. Determining fracture parameters with full-field optical methods. Exp Mech 1989;29:241–7.
[16] McNeill SR, Peters WH, Sutton MA. Estimation of stress intensity factor by digital image correlation. Eng Fract Mech 1987;28:101–12.
[17] Andanto-Buento J, Lambros J. Investigation of crack growth in functionally graded materials using digital image correlation. Eng Fract Mech 2002;69:1695–711.
[18] Yoneyama S, Takashi M. Automatic determination of stress intensity factor utilizing digitial image correlation. J Japanese Soc Exp Mech 2001;1:202–6.
[19] Kirugulige MS, Tippur HV. Measurement of fracture parameters for a mixed-mode crack driven by stress waves using image correlation technique and high-speed digital photography. Strain 2009;45:108–22.
[20] Kirugulige MS. A study of mixed-mode dynamic fracture in advanced particulate composites by optical interferometry, digital image correlation, and finite element methods. PhD Dissertation. Auburn University; 2007.
[21] Yoneyama S, Arikawa S, Kusayanagi S, Hazumi K. Evaluating J-integral from displacement fields measured by digital image correlation. Strain 2014;50:147–60.
[22] Yates JR, Zanganeh M, Tai YH. Quantifying crack tip displacement fields with DIC. Eng Fract Mech 2010;77:2063–76.
[23] Chong KP, Kuruppu MD. New specimen for fracture toughness determination for rock and other materials. Int J Fract 1984;26:R49–62.
[24] Chong KP, Kuruppu MD, Kuszmaul JS. Fracture toughness determination of rocks with core-based specimens. In: SEM/RILEM International Conference on Fracture of Concrete and Rocks, Texas; 1987.
[25] Lim IL, Johnston IW, Choi SK. Stress intensity factors for semi-circular specimens under three-point bending. Eng Fract Mech 1993;44(3):363–82.
[26] Owens AT, Tippur HV. Measurement of mixed-mode fracture characteristics of an epoxy-based adhesive using a hybrid Digital Image Correlation (DIC) and Finite Elements (FE) approach. Opt Lasers Eng 2021;140:106544.
[27] Blaber J, Adair B, Antoniou A. Ncorr: open-source 2D digital image correlation Matlab software. Exp Mech 2015;55(6):1105–22.
[28] He KSJTX. Guided image filtering. IEEE Trans Pattern Anal Mach Intell 2013;35(6):1397–409.
[29] Shih CF, Moran B, Nakamura T. Energy release rate along a three-dimensional crack front in a thermally stressed body. Int J Fract 1986;30:79–102.
[30] Shih CF, Asaro R. Elastic-plastic analysis of cracks on bimaterial interfaces: Part I: Small scale yielding. J Appl Mech 1988;55(2):299–316.
[31] Westergaard HM. Bearing pressure and cracks. J Appl Mech 1939;6:49–53.
[32] ASTM D638-14 - Standard Test Method for Tensile Properties of Plastics. ASTM International, West Conshohocken, PA; 2014.
[33] ASTM D695-15 - Standard Test Method for Compression Properties of Rigid Plastics. ASTM International, West Conshohocken, PA; 2015.
[34] Mulliken AD, Boyce MC. Mechanics of the rate-dependent elastic-plastic deformation of glassy polymers from low to high strain rates. Int J Solids Struct 2006;43:1331–56.
[35] Jordan JL, Foley JR, Siviour CR. Mechanical Properties of Epon 826/DEA Epoxy (AFRL-RW-EG-TP-2008-7418). Air Force Research Laboratory; 2008.
[36] Lee D, Tippur HV, Bogert P. Experimental study of dynamic crack growth in unidirectional graphite/epoxy composites using digital image correlation method and high-speed photography. J Compos Mater 2009;43(19):2081–108.
[37] Lim IL, Johnston IW, Choi SK, Boland JN. Fracture testing of a soft rock with semi-circular specimens under three-point bending. Part 2 - Mixed-mode. Int J Rock Mech Min Sci 1994;31(3):199–212.
[38] Miller TC. Analysis of mixed-mode cracks in a rubbery particulate composite. Air Force Research Lab; 1998.
[39] Jamali J, Fan Y, Wood JT. The mixed-mode fracture behavior of epoxy by the compact tension shear test. Int J Adhes Adhes 2015;63:79–86.
[40] Kanchanomai C, Rattananon S, Soni M. Effects of loading rate on fracture behavior and mechanism of thermoset epoxy resin. Polym Test 2005;24:886–92.
[41] Kalthoff JF, Beinert J, Winkler S. Measurements of dynamic stress intensity factors for fast running and arresting cracks in double cantilever beam specimens. In: Fast Fracture and Crack Arrest, ASTM STP 627, G. T. G. T. Hahn and M. F. Kanninen, Eds., American Society for Testing and Materials; 1977. p. 161–176.
[42] Marur PR, Batra RC, Garcia G, Loos AC. Static and dynamic fracture toughness of epoxy/alumina composite with submicron inclusions. J Mater Sci 2004;39:1437–40.
[43] Joudon V, Portemond G, Lauro F, Bennani B. Experimental procedure to characterize the mode I dynamic fracture toughness of advanced epoxy resins. In: 4th International Conference of Impact Loading on Lightweight Structures (ICILLS 2014), Cape Town, South Africa; 2014.
[44] Pittman E, Koumlis S, Aung HN, Bellafatto A, Lamberson L. Rate-dependent fracture behavior of aerospace epoxies: PR-520 and 3502. J Aerospace Eng 2022;351.